

# We are IntechOpen, the world's leading publisher of Open Access books Built by scientists, for scientists

6,900

Open access books available

186,000

International authors and editors

200M

Downloads

Our authors are among the

154

Countries delivered to

TOP 1%

most cited scientists

12.2%

Contributors from top 500 universities



WEB OF SCIENCE™

Selection of our books indexed in the Book Citation Index  
in Web of Science™ Core Collection (BKCI)

Interested in publishing with us?  
Contact [book.department@intechopen.com](mailto:book.department@intechopen.com)

Numbers displayed above are based on latest data collected.  
For more information visit [www.intechopen.com](http://www.intechopen.com)



# Efficient Simulation of Airborne SAR Raw Data in Case of Motion Errors

*Yuhua Guo, Shichao Jin and Yuhong Guo*

## Abstract

In the simulation of SAR raw data, it is well-known that the frequency-domain algorithm is more efficient than a time-domain algorithm, making it is more suitable for extended scene simulation. However, the frequency-domain algorithm is perhaps better suited for ideal linear motion and requires some degrees of approximations to take the nonlinear motion effects. This chapter presents an efficient simulation approach based on hybrid time and frequency-domain algorithms under certain assumptions. The algorithm has high efficiency and is suitable for the simulation of extended scenes, which demands highly computational resources. The computational complexity of the proposed algorithm is analyzed, followed by numerical results to demonstrate the effectiveness and efficiency of the proposed approach.

**Keywords:** synthetic aperture radar (SAR), trajectory deviations, antenna pointing errors, raw data simulation, Fourier transform (FT)

## 1. Introduction

There are two major approaches to the SAR raw echo data simulation: time-domain and frequency-domain methods. For airborne SAR, the sensor platform trajectory, due to nonideal factors such as atmospheric turbulence, deviates from the linear motion state in the synthetic aperture time, which seriously affects the imaging quality if no proper compensation is made [1]. The time-domain algorithm can accurately reflect the influence of various error factors, but the pitfall is that the computational efficiency is low [2–4]. On the other hand, the frequency-domain algorithm, based on the two-dimensional frequency-domain expression of the original echo signal, uses a fast FT to realize simulation [5, 6]. This kind of algorithm delivers high efficiency to a high degree. However, it is only for simulation under ideal flight conditions.

The fast simulation of SAR imaging signals has a long history of research. The main idea of the existing methods is to realize the SAR raw data simulation in the frequency-domain with the high efficiency of the fast FT [7]. In recent years, Franceschetti's team in Italy has conducted a systematic study on the fast simulation algorithm of SAR raw data. A simulation method based on the two-dimensional frequency domain is proposed, which assumes slow platform motion with a narrow antenna beam [8]. Then, the algorithm is modified by introducing a one-dimensional azimuth Fourier transform and range time-domain integration [9].

Reference [10] improved the traditional 2-D frequency-domain method and extended it to the squint mode. However, these two algorithms only consider the case of the tracking error or the case of the squint mode and do not consider the case of the squint with the trajectory deviations. The time-frequency hybrid simulation methods were proposed to improve SAR raw echo data processing speed [11–20]. The original raw data is usually acquired in the squint situation due to the instability of the attitude. Furthermore, the change of antenna attitude will cause the change of beam direction, which leads to the degradation of image quality. The fast echo simulation algorithm for antenna attitude change has been proposed on the premise that the amplitude of linear antenna error is far less than the beam width [21–23]. For sinusoidal antenna azimuth attitude jitter, it will cause paired echoes. Similarly, sinusoidal antenna range attitude jitter will also cause paired echoes.

In this work, we present the fast echo simulation algorithm of trajectory offset and attitude jitter error. We first attempt to extend the Fourier domain approach to account for trajectory deviations at a non-zero squint angle. Then we consider the Fourier domain approach to account for trajectory deviations and antenna beam pointing errors, given rising more problematic for airborne SAR systems. The rest of the chapter is organized as follows: The algorithm for trajectory deviations is presented in Section 2. In Section 3, SAR signal simulations are carried out considering the trajectory deviations and antenna attitude variations. Finally, conclusions are drawn to close the chapter.

## 2. Raw echo algorithm of squint airborne strip SAR with trajectory offset error

In this section, an algorithm of raw echo with trajectory error in squint is proposed. The approach adopts the Acquisition Doppler (AD) [24] geometry instead of the standard cylindrical reference system (see **Figure 1**).

### 2.1 Raw echo algorithm of squint airborne strip SAR with trajectory offset error

The echo generation algorithm with trajectory error in squint is deduced by rotating the trajectory error along the line of sight. The motion error in the cone coordinate system is shown in **Figure 2**. The transformation relationship between a cylindrical coordinate system and a conical coordinate system is as follows:

$$r_0 = r \cos \phi, x_0 = x + r \sin \phi_d \quad (1)$$

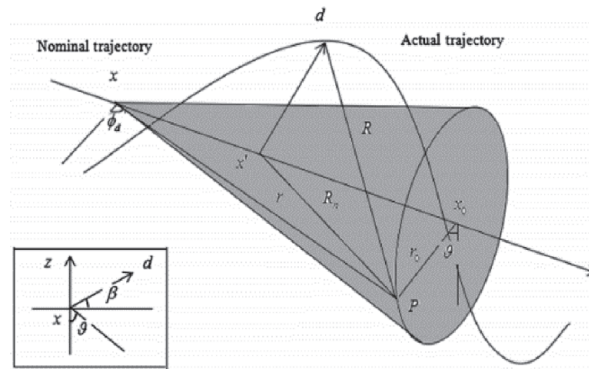


**Figure 1.**  
Geometric diagram of SAR with squint and trajectory offset.



where  $r'$  is the sampling coordinate of the range signal,  $\lambda$  is the wavelength,  $\gamma(x, r)$  is the reflection function,  $\text{rect}[\cdot]$  represents the rectangular envelope of the pulse. After applying the range FT of  $h(x', r')$ , we obtain

$$H(x', \eta) = \text{rect}\left[\frac{\eta}{2\alpha_r D}\right] \cdot \exp\left[j\frac{\eta^2}{4\alpha_r}\right] \times \iint dx dr \gamma(x, r) \quad (7)$$

$$\times \exp\left[-j\left(\eta + \frac{4\pi}{\lambda}\right) \cdot (r + \Delta R + \delta R)\right] \cdot \omega^2 \left(x' - x - r \frac{\sin(\phi - \phi_d)}{\cos \phi_d}\right)$$

Furthermore, by separating the factor  $\exp\left[-j\left(\eta + \frac{4\pi}{\lambda}\right)\delta r(x', \phi_d)\right]$ , we obtain

$$H(x', \eta) = \exp\left[-j\left(\eta + \frac{4\pi}{\lambda}\right)\delta r(x', \phi_d)\right] \tilde{H}(x', \eta) \quad (8)$$

where

$$\tilde{H}(x', \eta) = \text{rect}\left[\frac{\eta}{2\alpha_r D}\right] \cdot \exp\left[j\frac{\eta^2}{4\alpha_r}\right] \times \iint dx dr \gamma(x, r) \quad (9)$$

$$\times \exp\left[-j\left(\eta + \frac{4\pi}{\lambda}\right) \cdot (r + \Delta R(x', x, r, \phi_d) + \tilde{\psi}(x', r, \phi_d) + \tilde{\varphi}(x', x, r, \phi_d))\right]$$

$$\times \omega^2 \left(x' - x - r \frac{\sin(\phi - \phi_d)}{\cos \phi_d}\right)$$

If the following conditions are satisfied:

$$|\tilde{\varphi}(x', x, r, \phi_d)| \ll \frac{\lambda}{4\pi} \quad (10)$$

$$|\tilde{\psi}(x', x, r, \phi_d)| \ll \frac{f}{\Delta f} \frac{\lambda}{2\pi} \quad (11)$$

we can obtain the azimuth FT of  $\tilde{H}(x', \eta)$  as follows:

$$\begin{aligned} \tilde{H}(\xi, \eta) &= \int dr \exp[-j\bar{\eta}r] \int dr G(\xi - l, \eta, r) \Gamma(\xi - l, r) Q_\eta(l, \eta, r) \\ &= \int dr \exp[-j\bar{\eta}r] \{Q_\eta(\xi, \eta, r) \otimes_\xi [G(\xi, \eta, r) \Gamma(\xi, r)]\} \end{aligned} \quad (12)$$

where

$$Q_\eta(l, \eta, r) = FT_{x'}\{\exp[-j\bar{\eta}\tilde{\psi}(x', r, \phi_d)]\} \quad (13)$$

with  $\bar{\eta} = \eta + \frac{4\pi}{\lambda}$ , After evaluating  $\tilde{H}(\xi, \eta)$ , it can be direct get  $\tilde{H}(x', \eta)$  by using the inverse FT of  $\tilde{H}(\xi, \eta)$  along the azimuth direction. Then, using Eq. (8) and the range inverse FT, the original echo signal can be computed. The flowchart of the algorithm is shown in **Figure 3**. The validity of the range needs to satisfy Eqs. (10) and (11).

## 2.2 Computational complexity of the algorithm

Let us now consider the computational complexity of the algorithm in **Figure 3**. Suppose the data size is  $N_a \times N_r$ , with  $N_a$  corresponding to the number of azimuth

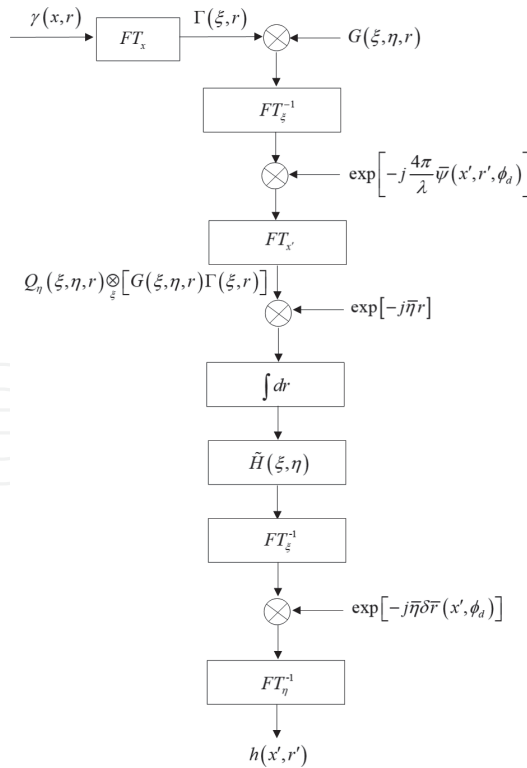


**Figure 3.**  
 Raw data simulation process of strip squint SAR with trajectory error.

sampling points, and  $N_r$  to the number of range sampling points. It follows that the amount of computation required by the algorithm is

$$N \approx N_a N_{r2} (3 + \log_2 N_a) + N_a N_r \left( 1 + \log_2 N_a + \frac{1}{2} \log_2 N_r \right) \quad (14)$$

$$\approx N_a N_r^2 (3 + \log_2 N_a)$$

Recalled that the required computation of time domain algorithm is as follows

$$\tilde{N} \approx N_a N_r N_{tp} N_{sa} \quad (15)$$

where  $N_{tp}$  is the size of the emitted pulse and  $N_{sa}$  is the synthetic aperture,  $N_{tp}$  is usually equal to the size of  $N_r$ . The ratio of Eqs. (14) and (15) takes the form

$$\frac{\tilde{N}}{N} \approx \frac{N_{sa}}{3 + \log_2 N_a} \quad (16)$$

It is evident that compared with the time domain simulation method, the proposed method has higher computational efficiency.

### 2.3 Algorithm simulation verification

In what follows, we use the SAR system parameters listed in **Table 1** to verify the SAR raw data simulation algorithm of non-ideal track under squint condition. **Figure 4** shows the track deviation between the actual track and the ideal track. For a point target located at the near range  $r = (4840 / \cos 4^\circ) m$ , the phase difference between the simulated and the exact raw signal, along the range direction and the azimuth direction, is displayed in **Figure 5(a)** and **(b)**, respectively. We see that the



Nominal height	4000 m	Range pixel dimension	3 m
Midrange coordinate	5140 m	Chirp bandwidth	45 MHz
Wavelength	3.14 cm	Chirp duration	5 μs
Pulse Repetition Frequency	400 Hz	Velocity	100 m/s
Sampling Frequency	50 MHz	Number of azimuth samples of the raw data	972
Azimuth pixel dimension	25 cm	Number of range samples of the raw data	416

Table 1.  
Simulation parameters.

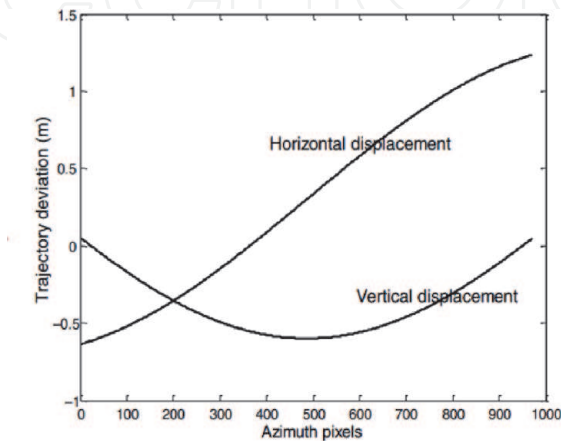


Figure 4.  
Sensor displacements.

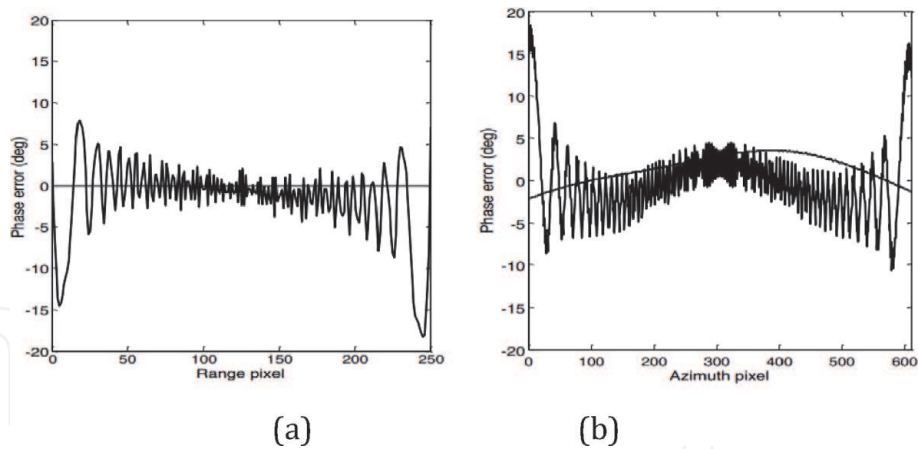
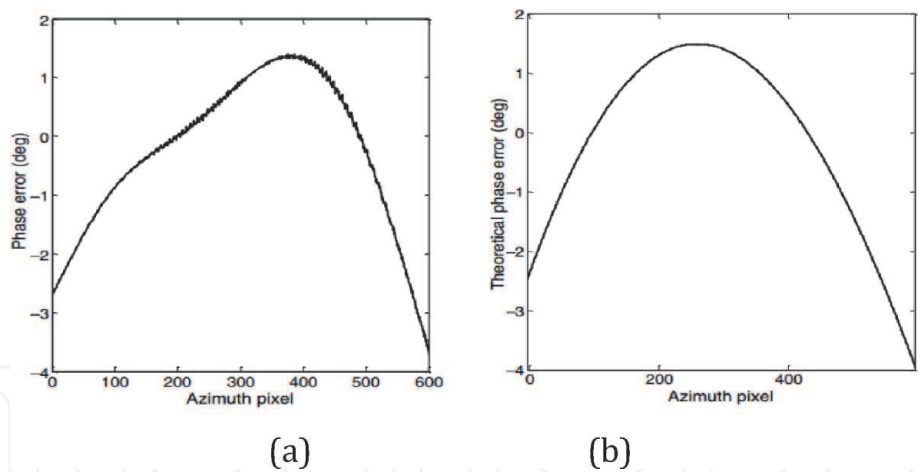
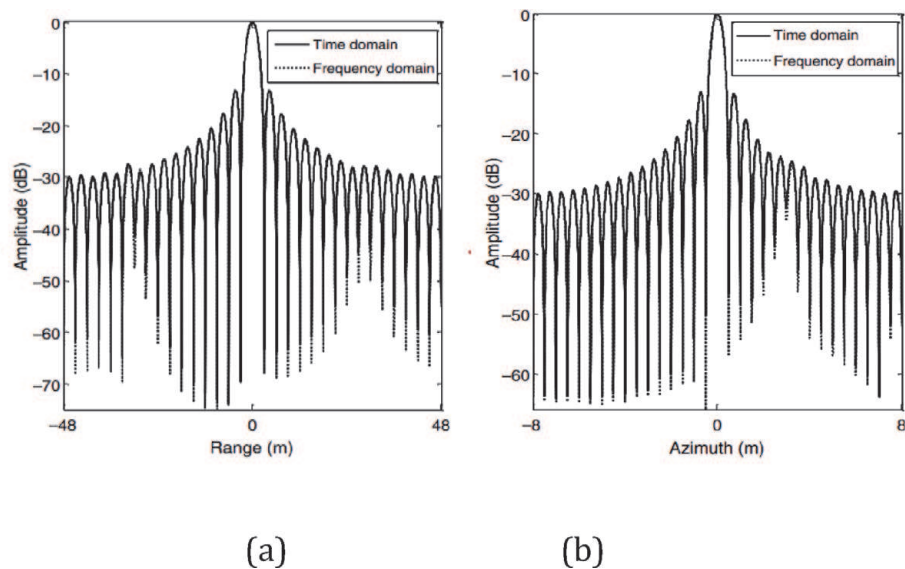


Figure 5.  
(a) Range cut, (b) azimuth cut, the point target is located in the close range position ( $r = (4840 / \cos 4^\circ) \text{ m}$ ) of the scene.

phase error is much smaller than  $\pi/10$ , which in practice is negligible. By comparing the “depurated” phase error and the expected phase error  $(4\pi/\lambda)\tilde{\varphi}(x',x,r,\phi_d)$  (see **Figure 6**), we may conclude that the azimuth “depurated” phase error is given rise by the approximation of Eq. (10). Moreover, the point target impulse response for midrange at squint angle  $15^\circ$  after the motion compensation are shown in **Figure 7 (a)** and **(b)**. In addition, the figure of merits by point target analysis for midrange shown in **Figure 7(a)** and **(b)** between the proposed approach and the time-domain one is given in **Table 2**. The proposed raw data generator has high precision at least as that by the time domain algorithm.



**Figure 6.**  
(a) The phase error (smooth line) after removing the stationary phase influence. (b) the phase error along the azimuth direction ( $r = (4840 / \cos \phi_d) m$ ) according to the formula  $|\varphi(x', x, r, \phi_d)| < \frac{4\pi}{\lambda}$ .



**Figure 7.**  
Point target imaging results after motion error compensation. (a) Range cut and (b) azimuth cut.

Simulation method	Azimuth direction			Range direction		
	IRW (m)	PSLR (dB)	ISLR (dB)	IRW (m)	PSLR (dB)	ISLR (dB)
Time domain simulation algorithm	0.2344	-13.1035	-9.6665	2.8125	-13.2115	-9.6759
Simulation algorithm of squint with trajectory offset	0.2344	-13.2322	-9.6862	2.8125	-13.2160	-9.6871

**Table 2.**  
Point target evaluation results.

Finally, the extended scene is considered. The final results are given in **Figure 8**, where **Figure 8(a)** shows the image without motion compensation, **Figure 8(b)** displays the results by a two-step MOCO algorithm, and **Figure 8(c)** is the image after the motion compensation [25]. Concerning the computational efficiency, it took only about 2 min for the simulation run, as shown in **Figure 8(c)**, on an 8-GHz Intel Core i5 personal computer.



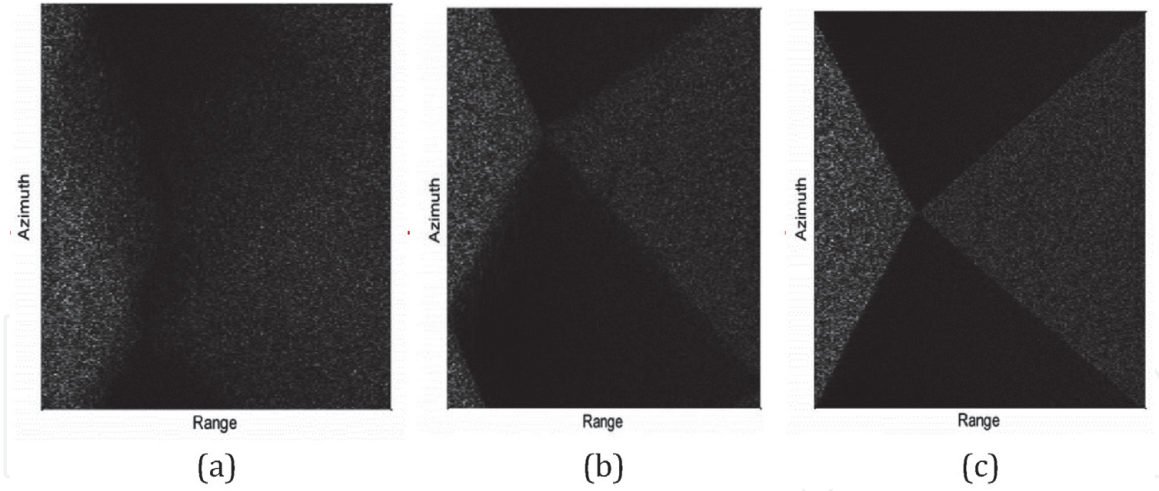


**Figure 8.**

Comparison of imaging results: (a) No motion compensation, (b) second order motion error compensation, (c) the compensation method in ref. [25] is used.

### 3. Raw echo algorithm of airborne stripmap SAR with trajectory error and attitude jitter

Due to the air disturbance or the flight instability of the SAR platform, the platform trajectory deviation and attitude error are inevitably introduced into the sensor parameters. This section considers the raw echo algorithm of airborne stripmap SAR with trajectory error and attitude jitter.

#### 3.1 Raw echo algorithm of airborne stripmap SAR with trajectory error and attitude jitter

Firstly, the simulation algorithm of antenna beam pointing error is briefly introduced. In Ref. [22], a two-dimensional frequency-domain echo simulation algorithm is proposed to reflect the beam pointing error. The difference between the raw data echo, including antenna beam pointing error, and ideal echo is the azimuth envelope. When the amplitude of the antenna beam jitter is less than the beam width, the azimuth amplitude weighting function can be approximated by the Taylor expansion. From reference [22], When the beam pointing is sinusoidal jitter, a pair of echoes is erroneously produced.

Suppose the received echo is as follows:

$$h(x', r') = \iint dx dr \gamma(x, r) \cdot \exp \left\{ -j \frac{4\pi}{\lambda} R - j \frac{4\pi}{\lambda} \frac{\Delta f}{f} \frac{1}{c\tau} (r' - R)^2 \right\} \times \text{rect} \left[ \frac{r' - R}{c\tau/2} \right] \cdot W^2 \left[ \frac{x' - x - \delta_x}{X} \right] \quad (17)$$

where  $\delta_x = (r + \delta r_{xr}(x', x, r, \phi_d)) \tilde{\delta}_{az}(x')$  is the antenna pointing error in azimuth direction. When the amplitude of antenna beam jitter is less than the beam width, the azimuth amplitude weighting function is approximated by the second-order Taylor expansion:

$$W^2 \left( \frac{x' - x - \delta_x}{X} \right) \approx W^2 \left( \frac{x' - x}{X} \right) - W^{2(1)} \left( \frac{x' - x}{X} \right) (r + \delta r_{xr}(x', x, r)) \delta_{az}(x') + \frac{1}{2} W^{2(2)} \left( \frac{x' - x}{X} \right) (r + \delta r_{xr}(x', x, r))^2 \delta_{az}^2(x') \quad (18)$$

where  $r$  is the distance coordinate between the platform and the target point, and the original echo is decomposed into three parts:

$$h(x', r') \approx h_0(x', r') + h_1(x', r') + h_2(x', r') \quad (19)$$

where  $h_0(x', r')$  is equivalent to the original echo with trajectory deviations, which can be calculated by the traditional frequency-domain algorithm. The last two terms of Eq. (19) contain trajectory offset error and antenna attitude jitter error.  $h_0(x', r')$  can be estimated by echo simulation algorithm, which only contains trajectory offset error. Therefore, the main task is to evaluate the two terms of  $h_1(x', r')$  and  $h_2(x', r')$ .

In order to expand the range of distance effectiveness, we assume that

$$\bar{f}_1(x, x', \eta, r) \approx (r + \delta r_r(x', r)) \cdot \gamma(x, r) \cdot \exp \left\{ -j \frac{4\pi}{\lambda} \psi(x', r) \right\} \quad (20)$$

which satisfies the following condition:  $\left| \left( \eta + \frac{4\pi}{\lambda} \right) \varphi(x', x, r) + \eta \psi(x', r) \right| \ll 1$ . The azimuth Fourier transform of  $\bar{f}_1$  can be expressed as:  $\bar{F}_1(\chi, l, \eta, r) = \Gamma(\chi, r) Q_1(l, r)$ . where  $\Gamma(\cdot)$  is the azimuth FT of  $\gamma(x, r)$ .

$$Q_1(l, r) = FT_{x'} \left\{ (r + \delta r_r(x', r)) \cdot \exp \left[ -j \frac{4\pi}{\lambda} \psi(x', r) \right] \right\} \quad (21)$$

Then  $\bar{H}(\xi, \eta) = \int \exp[-j\bar{\eta}r] \left\{ Q_1(\xi, r) \otimes_{\xi} [G(\xi, \eta, r) \cdot \Gamma(\xi, r)] \right\} dr$ .

The system function  $G(\cdot)$  of SAR is decomposed into two parts

$$G(\xi, \eta, r) = G_{A1}(\xi, r) \cdot G_{B1}(\xi, \eta, r) \quad (22)$$

where the term.

$G_{A1}(\xi, r) = \exp \left[ -j \left( \sqrt{\left( \frac{4\pi}{\lambda} \right)^2 - \xi^2} - \frac{4\pi}{\lambda} \right) r \right]$  describes the azimuth frequency modulation, including the change of focusing depth, and

$$\begin{aligned} G_{B1}(\xi, \eta, r) = & \text{rect} \left[ \frac{\eta}{2bc\tau/2} \right] \cdot \left( \frac{PRF}{v} \right) \cdot \left[ W^2 \left( \frac{\xi - \Delta\xi}{2\Omega_r} \right) - W^2 \left( \frac{\xi}{2\Omega_r} \right) \right] \exp \left\{ j \frac{\eta^2}{4b} \right\} \\ & \times \exp \left\{ -j \left( \sqrt{\bar{\eta}^2 - \xi^2} - \bar{\eta} \right) r \right\} \cdot \exp \left\{ -j \left( \sqrt{\left( \frac{4\pi}{\lambda} \right)^2 - \xi^2} - \frac{4\pi}{\lambda} \right) r \right\} \end{aligned} \quad (23)$$

the migration effect of range element and the error of antenna beam jitter. Then, we have

$$\tilde{h}_1(\xi, \eta) \approx \int \exp \{ -j\bar{\eta}r \} \cdot G_{B1}(\xi, \eta, r) \cdot \{ Q_1(\xi, r) \otimes_{\xi} [G_A(\xi, r) \cdot \Gamma(\xi, r)] \} dr \quad (24)$$

Similarly, let

$$\bar{f}_2(x, x', \eta, r) \approx \frac{1}{2} (r + \delta r_r(x', r))^2 \cdot \gamma(x, r) \cdot \exp \left\{ -j \frac{4\pi}{\lambda} \psi(x', r) \right\} \quad (25)$$

and

$$Q_2(\xi, r) = FT_{x'} \left\{ \frac{1}{2} (r + \delta r_r(x', r))^2 \cdot \exp \left[ -j \frac{4\pi}{\lambda} \psi(x', r) \right] \right\} \quad (26)$$

$$\begin{aligned} G_{B2}(\xi, \eta, r) = & \text{rect} \left[ \frac{\eta}{2bc\tau/2} \right] \cdot \left( \frac{PRF}{v} \right)^2 \cdot \left[ W^2 \left( \frac{\xi}{2\Omega_x} \right) - 2W^2 \left( \frac{\xi - \Delta\xi}{2\Omega_x} \right) \right. \\ & \left. + W^2 \left( \frac{\xi - 2\Delta\xi}{2\Omega_x} \right) \right] \times \exp \left\{ j \frac{\eta^2}{4b} \right\} \cdot \exp \left\{ -j \left( \sqrt{\bar{\eta}^2 - \xi^2} - \bar{\eta} \right) r \right\} \\ & \times \exp \left\{ j \left( \sqrt{\left( \frac{4\pi}{\lambda} \right)^2 - \xi^2} - \frac{4\pi}{\lambda} \right) r \right\} \end{aligned} \quad (27)$$

we yield

$$\tilde{h}_2(\xi, \eta) \approx \int \exp[-j\bar{\eta}r] \cdot G_{B2}(\xi, \eta, r) \times \{Q_2(\xi, r) \otimes_\xi [G_A(\xi, r)\Gamma(\xi, r)]\} dr \quad (28)$$

From Eqs. (24) and (28), we obtain the efficient computation of  $\tilde{h}_1(\xi, \eta)$  and  $\tilde{h}_2(\xi, \eta)$ . **Figure 9** summarizes the computation flow chart of the procedures outlined above. Finally,  $h(x', r')$  can be evaluated from **Figure 10**. The effectiveness of the algorithm for antenna jitter is  $\delta_{az}(x') \ll \frac{X}{r + \delta r_r(x', r)} < \frac{X}{r} = \frac{\lambda}{L}$ .

Note that the trajectory deviations should satisfy the following condition:

$$\left| \left( \eta + \frac{4\pi}{\lambda} \right) \varphi(x', x, r) + \eta \psi(x', r) \right| \ll 1 \quad (29)$$

which ensures that the range of distance effectiveness of the algorithm.

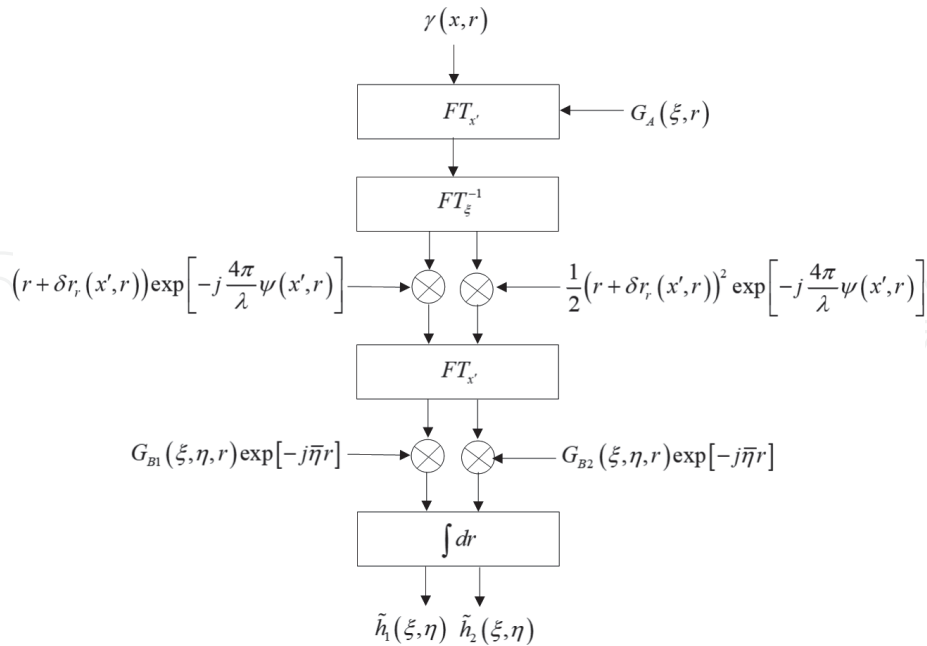


**Figure 9.**  
Flowchart of the simulation.

### 3.1.1 Computational complexity

The complexity of algorithms given in Section 3.1 increases with the order of antenna pattern decomposition. Suppose  $N_a$  and  $N_r$  are the azimuth and range pixel

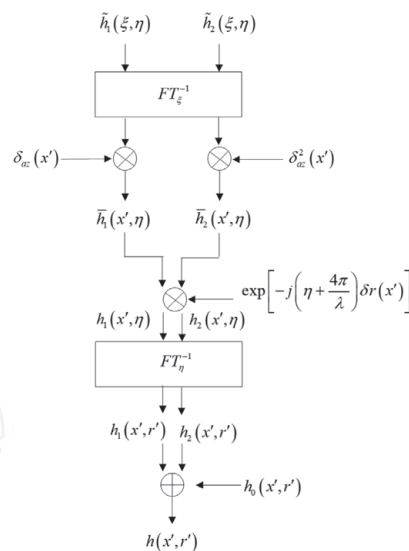


**Figure 10.**  
Horizontal and vertical components of medium trajectory offset error.

size of the original signal,  $N_a N_r$  is the computational complexity of  $\gamma(x, r)$ . Let  $\tilde{N}$  and  $N$  be the computational complexity of 3.1 part and medium trajectory offset error algorithm, then  $\tilde{N} = (n + 1)N$ , where  $N = N_x N_r^2$ . Now we compare the computational complexity of part 3.1 and the exact time domain algorithm. It is known that the computational complexity of time domain is  $\hat{N} = N_x N_r N_{tp} N_{sa}$ , where  $N_{tp}$  and  $N_{sa}$  are the sizes of the emitted pulse and the synthetic aperture. Generally,  $n$  is less than  $N_{sa}$  and  $N_{tp}$  are the same size with  $N_r$ . Then the algorithm given in this part is more efficient than the time-domain algorithm. The calculation time-saving rate is

$$\frac{\hat{N}}{\tilde{N}} \approx \frac{N_{sa}}{n + 1} \tag{30}$$

Therefore, the algorithm given in Section 3.1 can simulate the extended scene in a reasonable time.

### 3.1.2 Algorithm verification

In this part, we will give some simulation results to verify the proposed algorithm. The simulation parameters are selected from the X-band SAR data in Ref.s [8, 9], and the main parameters are shown in **Table 3**. Note that the precise time domain simulation can be obtained from Eq. (17). In order to simplify, the algorithm given in part 3.1 is called algorithm A, and the time-domain algorithm is

Nominal height	4000 m	Range pixel dimension	3 m
Midrange coordinate	5140 m	Chirp bandwidth	45 MHz
Wavelength	3.14 cm	Chirp duration	5 $\mu$ s
Pulse Repetition Frequency	400 Hz	Azimuth antenna dimension	1 m
Sampling Frequency	50 MHz	Number of azimuth samples in the raw data	1941
Azimuth pixel dimension	25 cm	Number of range samples in the raw signals	830

**Table 3.**  
Sensor simulation parameters.

called algorithm B. Let a single point target be located in the middle of the scene ( $r = 5140$  m), and the horizontal and vertical components are shown in **Figure 11**. Let the antenna pointing error be as follows:

$$\delta_a(x') = \delta_m \sin \left( \frac{2\pi}{vT_b} x' + \varphi_0 \right) \quad (31)$$

where  $\delta_m$  is the amplitude,  $T_b$  is the period of antenna jitter and  $\varphi_0$  is the initial phase. Assumptions  $\delta_m = \frac{1}{20} \frac{\lambda}{L}$ ,  $T_b = \frac{1}{10} T_s$  and  $\varphi_0 = 0$ . **Figure 11** shows the horizontal and vertical components of the trajectory offset, and the antenna pointing error is Eq. (31). Now we consider the near range point ( $r = 4840$  m) in the scene. The amplitude and phase comparison results of algorithms A and B are shown in **Figures 12** and **13**, respectively. Similar conclusion can be drawn that the amplitude error and phase error of algorithm A and B are very small, which verifies the effectiveness of algorithm A. **Table 4** shows the imaging quality evaluation results of algorithms A and B at near range ( $r = 4840$  m), center range ( $r = 5140$  m) and far range ( $r = 5440$  m), including impulse response width (IRW), peak sidelobe ratio (PSLR) and integral sidelobe ratio (ISLR).

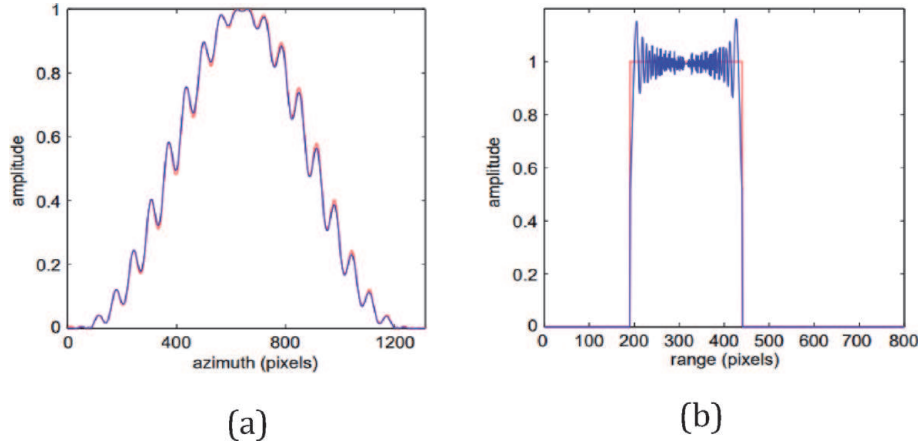


**Figure 11.** Amplitude comparison results of algorithm A and B (the blue line represents algorithm A and the red line represents algorithm B) (a) azimuth cut. (b) Range cut. The point target is located in the scene, and the close range  $R = 4840$  meters.

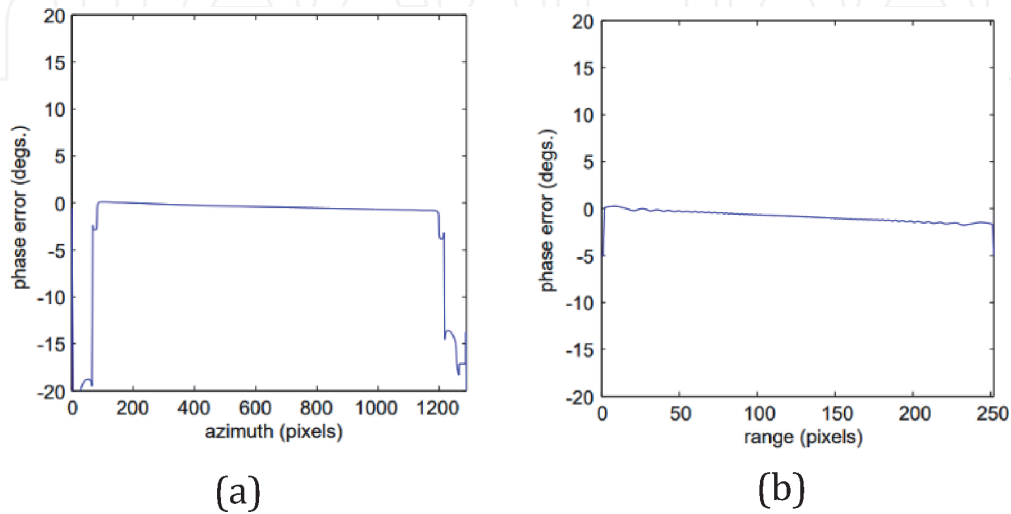


**Figure 12.** Phase comparison results of algorithm A and algorithm B. (a) Azimuth cut. (b) Range cut. The point target is located in the scene, and the close range  $R = 4840$  meters.

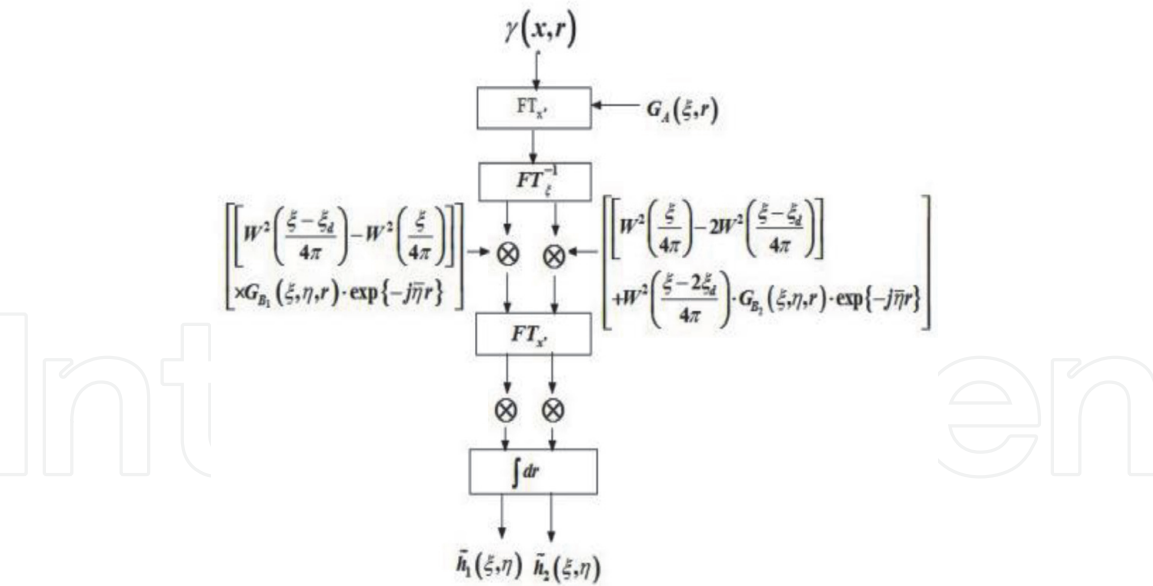


**Figure 13.**  
Flowchart of medium trajectory error and attitude jitter at squint angle.

Algorithm	r (m)	Azimuth direction			Range direction		
		IRW (dB)	PSLR (dB)	ISLR (dB)	IRW (dB)	PSLR (dB)	ISLR (dB)
A	4840	0.2266	−5.0346	−3.9095	−2.7188	−6.8351	−5.6503
	5140	0.2227	−3.4025	−2.2344	2.8125	−12.3214	−9.5441
	5440	0.2188	−2.4523	−1.2622	2.7656	−8.5	−7.2288
B	4840	0.2266	−5.3933	−4.2801	2.7656	−7.1473	−6.0101
	5140	0.2227	−3.3611	−2.1945	2.7656	−12.8208	−9.6497
	5440	0.2188	−2.4399	−1.2496	2.7656	−8.0237	−6.8483

**Table 4.**  
The focus performance of the point target response of algorithm A and B.

**3.2 Raw echo algorithm of airborne stripmap SAR with trajectory error and attitude jitter under squint conditions**

This section presents the simulation algorithm of airborne SAR raw echo with trajectory offset and attitude jitter error under squint conditions.

**3.2.1 Simulation algorithm**

Suppose the received echo is as follows:

$$h(x', r') = \iint dx dr \gamma(x, r) \cdot \exp \left\{ -j \frac{4\pi}{\lambda} R - j \frac{4\pi}{\lambda} \frac{\Delta f}{f} \frac{1}{c\tau} (r' - R)^2 \right\} \times \text{rect} \left[ \frac{r' - R}{c\tau/2} \right] \cdot W^2 \left[ \frac{x' - x - \delta_x}{X} \right] \tag{32}$$

where  $\delta_x = (r + \delta \bar{r}_{xr}(x', x, r, \phi_d)) \tilde{\delta}_{az}(x')$  is the antenna pointing error in azimuth direction. From [25] we have



$$\begin{aligned}
\delta \bar{r}_{xr}(x', x, r, \phi_d) \approx & d(x') (\sin \beta(x') \cos \phi_d \cos \vartheta(x, r) - \cos \beta(x') \sin \vartheta(x, r) \\
& + \frac{1}{2} (\sin \phi_d)^2 (\cos \vartheta(x, r))^2 \sin \beta(x') \cos \phi_d \cos \vartheta(x, r) + \frac{1}{2} \cos \beta(x') \\
& \times \sin \vartheta(x, r) (\sin \phi_d)^2 (\cos \vartheta(x, r))^2)
\end{aligned} \quad (33)$$

Eq. (32) is a signal model for the exact time-domain simulation and can be used as the criterion to judge the validity of the algorithm proposed below.

When the beam pointing error is less than the beam width, the antenna pattern can be approximated as follows:

$$\begin{aligned}
W^2 \left( \frac{x' - x - \delta_{x'}}{X} \right) \approx & W^2 \left( \frac{x' - x}{X} \right) - W^{2(1)} \left( \frac{x' - x}{X} \right) (r + \delta \bar{r}_{xr}(x', x, r, \phi_d)) \delta_{az}(x') \\
& + \frac{1}{2} W^{2(2)} \left( \frac{x' - x}{X} \right) (r + \delta \bar{r}_{xr}(x', x, r, \phi_d))^2 \delta_{az}^2(x')
\end{aligned} \quad (34)$$

where  $W^{2(n)}(\cdot)$  is the  $n$ th derivative of the antenna pattern. Accordingly, the echo can be decomposed as follows:

$$h(x', r') \approx \hat{h}_0(x', r') + \hat{h}_1(x', r') + \hat{h}_2(x', r') \quad (35)$$

The above equation,  $\hat{h}_0(x', r')$  only includes trajectory deviations, the latter two terms including trajectory offset and attitude jitter.

Assuming that the range Fourier transform of  $\hat{h}_1(x', r')$  is  $\hat{h}_1(x', \eta)$ , then

$$\hat{h}_1(x', \eta) = \exp \left[ -j \left( \eta + \frac{4\pi}{\lambda} \right) \delta \bar{r}(x', \phi_d) \right] \bar{\hat{h}}_1(x', \eta) \quad (36)$$

The term  $\bar{\delta}_{az}(x')$  can be extracted from the integral, that is

$$\bar{\hat{h}}_1(x', \eta) = \bar{\delta}_{az}(x') \tilde{\hat{h}}_1(x', \eta) \quad (37)$$

$$\begin{aligned}
\hat{h}_1(x', \eta) = & \text{rect} \left[ \frac{\eta}{bct} \right] \exp \left\{ j \frac{\eta^2}{4b} \right\} \iint dx dr \gamma(x, r) \exp \left\{ -j \left( \eta + \frac{4\pi}{\lambda} \right) \right. \\
& \times (r + \Delta R(x' - x, r) + \bar{\psi}(x', r, \phi_d) + \bar{\varphi}(x', x, r, \phi_d)) \\
& \times [-(r + \delta \bar{r}_{xr}(x', x, r, \phi_d))] W^{2(1)} \left( \frac{x' - x}{X} \right)
\end{aligned} \quad (38)$$

The azimuth Fourier transform of  $\tilde{\hat{h}}_1(x', \eta)$  is

$$\bar{\hat{h}}_1(\xi, \eta) = FT[\bar{\delta}_{az}(x')] \otimes \tilde{\hat{h}}_1(\xi, \eta) \quad (39)$$

where

$$\tilde{\hat{h}}_1(\xi, \eta) = \int dr \exp[-j\eta r] \int dl \tilde{G}_1(\xi - l, \eta, r) \tilde{\hat{F}}_1(\xi - l, l, \eta, r) \quad (40)$$

$\tilde{\hat{F}}_1(\cdot)$  is the Fourier transform of  $\tilde{f}_1(\cdot)$ , and

$$\begin{aligned}
\tilde{f}_1(x, x', \eta, r) = & -[r + \delta \bar{r}_{xr}(x', x, r, \phi_d)] \gamma(x, r) \\
& \times \exp \left\{ -j \left( \eta + \frac{4\pi}{\lambda} \right) [\bar{\psi}(x', r, \phi_d) + \bar{\varphi}(x', x, r, \phi_d)] \right\}
\end{aligned} \quad (41)$$

Similarly, a two-dimensional Fourier transform  $\hat{h}_2(x', r')$  can be obtained. By performing a range FT of  $h_2(x', r')$  and separating the factor  $\exp \{-j\eta\delta\bar{r}(x', \phi_d)\}$ , we get  $\bar{h}_2(x', \eta)$ . Then, after azimuth FT of  $\bar{h}_2(x', \eta)$ , we obtain:  $\bar{h}_2(\xi, \eta) = FT_{x'} [\delta_{az}^2(x')] \otimes \tilde{h}_2(\xi, \eta)$ , where

$$\tilde{h}_2(\xi, \eta) = \int dr \exp [-j\eta\bar{r}] \int dl \tilde{G}_2(\xi - l, \eta, r) \tilde{F}_2(\xi - l, l, \eta, r) \quad (42)$$

where  $\tilde{F}_2(\cdot)$  is the two-dimensional FT of  $\tilde{f}_2(\cdot)$ . The difference between  $\tilde{f}_1(\cdot)$  and  $\tilde{f}_2(\cdot)$  is that the former contains a factor  $[r + \delta\bar{r}_{xr}(x', x, r, \phi_d)]$  while the latter contains a factor  $\frac{1}{2}[r + \delta\bar{r}_{xr}(x', x, r, \phi_d)]^2$ . If the two-dimensional spectrum of  $\tilde{h}_1(\xi, \eta)$  and  $\tilde{h}_2(\xi, \eta)$  is obtained from Eqs. (40) and (42), then the estimation of  $h(x', r')$  can be obtained from **Figure 14**. However, due to the coupling of azimuth and distance between  $\tilde{f}_1(\cdot)$  and  $\tilde{f}_2(\cdot)$ , it is necessary to decouple them. Therefore, we adopt the following approach:

The amplitude approximation  $\tilde{f}_1(\cdot)$  and  $\tilde{f}_2(\cdot)$  satisfy the following conditions:  
 $\delta\bar{r}_{xr}(x', x, r, \phi_d) \approx \delta\bar{r}(x', r, \phi_d)$ . Phase approximation needs to meet the following requirements:

$$\tilde{f}_1(\cdot) \approx (r + \delta\bar{r}_{xr}(x', r, \phi_d))\gamma(x, r) \exp \left\{ -j\frac{4\pi}{\lambda}\bar{\psi}(x', r, \phi_d) \right\} \quad (43)$$

$$\tilde{f}_2(x, x', \eta, r) \approx \frac{1}{2}(r + \delta\bar{r}_r(x', r, \phi_d))^2\gamma(x, r) \times \exp \left[ -j\frac{4\pi}{\lambda}\bar{\psi}(x', r, \phi_d) \right] \quad (44)$$

$$|\bar{\varphi}(x', x, r, \phi_d)| < < \frac{\lambda}{4\pi} \quad (45)$$

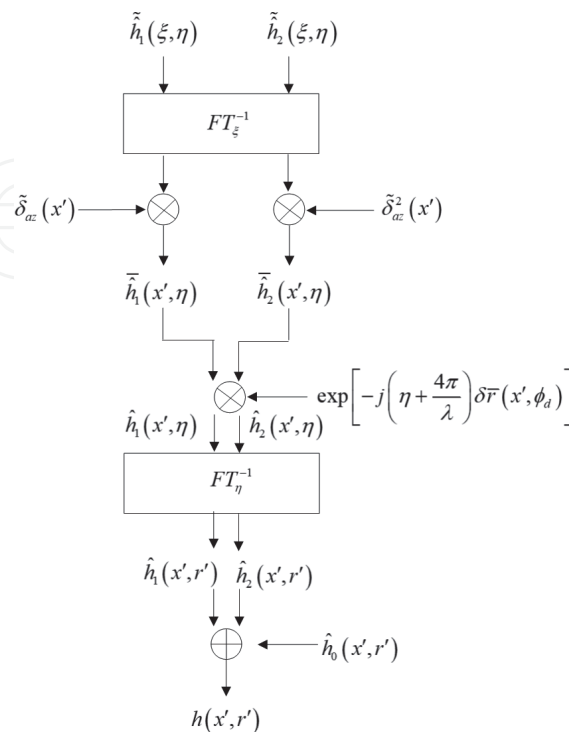


**Figure 14.**  
 SAR raw data echo simulation diagram.

$$|\bar{\psi}(x', r, \phi_d)| < \frac{f}{\Delta f} \frac{\lambda}{2\pi} \quad (46)$$

then

$$\begin{aligned} \tilde{h}_1(\xi, \eta) &= \int \exp(-j\bar{\eta}r) \int dl G_1(\xi - l, \eta, r) \Gamma(\xi - l, r) Q(l, \eta, r) \\ &= \int dr \exp(-j\bar{\eta}r) \{ Q(\xi, \eta, r) \otimes_{\xi} [G_1(\xi, \eta, r) \Gamma(\xi, r)] \} \end{aligned} \quad (47)$$

where

$$Q(l, \eta, r) = FT_{x'} \{ \exp[-j\bar{\eta}\bar{\psi}(x', r, \phi_d)] \} \quad (48)$$

$$\begin{aligned} G_1(\xi, \eta, r) &\approx \text{rect}\left(\frac{\eta}{bc\tau}\right) \left[ W^2\left(\frac{\xi - \xi_d - \Delta\xi(r)}{2a}\right) - W^2\left(\frac{\xi - \xi_d}{2a}\right) \right] \\ &\times \exp\left(j\frac{\eta^2}{4b}\right) \exp\left[-j\left(\sqrt{\bar{\eta}^2 - \xi^2} \cos \phi_d - \bar{\eta}\right)r - j\xi r \sin \phi_d\right] \end{aligned} \quad (49)$$

Similarly, we can get an estimate of  $\tilde{h}_2(\xi, \eta)$ , with the flow chart shown in **Figure 15**.

In the simulation, the attitude change needs to meet the following condition:

$$\delta_{az}(x') \ll \frac{X}{r + \delta\bar{r}_r(x', r, \phi_d)} < \frac{X}{r} = \frac{\lambda}{L} \quad (50)$$

Combined with conditions (45) and (46), we see that the algorithm is suitable for squint with medium trajectory offset error and antenna beam pointing error.

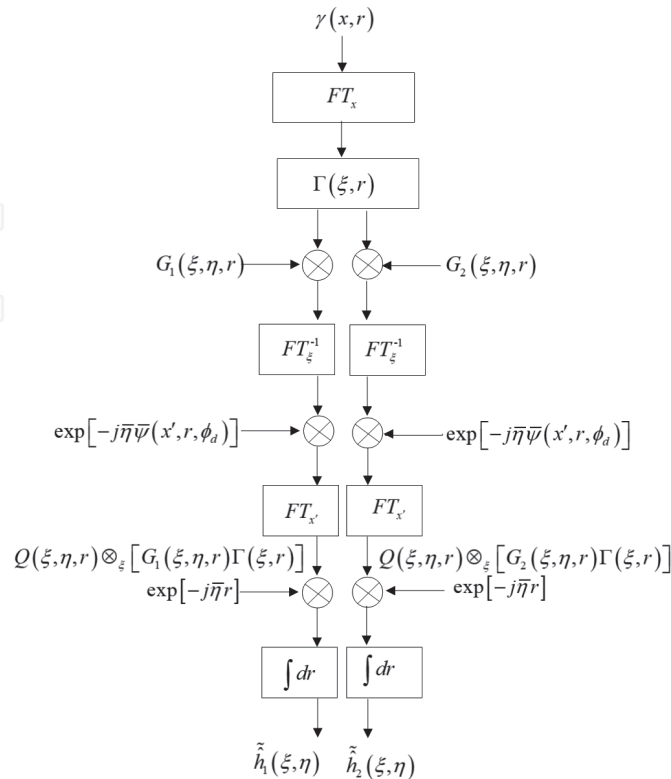


**Figure 15.**  
The flowchart of medium trajectory error and attitude jitter.

The computational efficiency of the algorithm is analyzed below. Obviously, the computational complexity of the algorithm increases with the expansion order of the antenna pattern. Let  $N$  be the computational complexity with

$$N \approx n N_a N_r^2 (3 + \log_2 N_a) \tag{51}$$

and  $\tilde{N}$  be the computational complexity of the time domain method. It turns out that the following ratio is obtained

$$\frac{\tilde{N}}{N} \approx \frac{N_{sa}}{n(3 + \log_2 N_a)} \tag{52}$$

We observe from the above equation that the proposed algorithm has higher computational efficiency than the time-domain algorithm for the same order of antenna pattern expansion  $n$ .

3.2.2 Simulation results

In this section, the proposed algorithm is verified by comparing with the simulation results of time-domain algorithm. The trajectory offset error is shown in **Figure 16** and the antenna pointing error is given by Eq. (31). **Figure 17** shows the phase comparison results of azimuth and range directions, where **Figure 17(a)** is

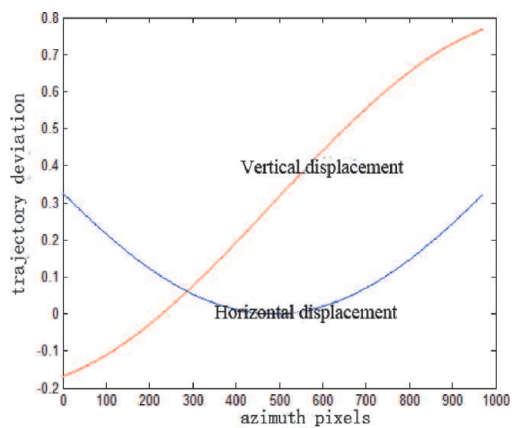


**Figure 16.**  
Moderate trajectory deviations [m] vs. the azimuth pixels.

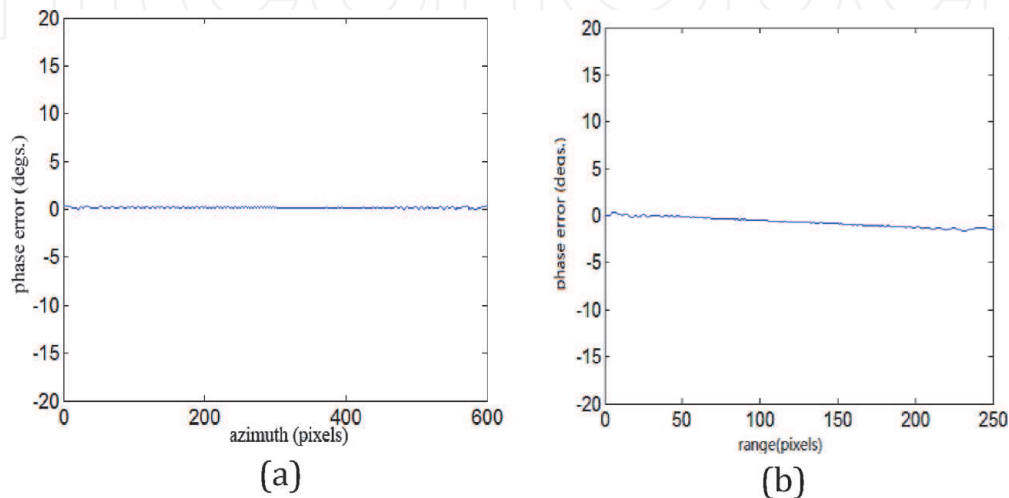


**Figure 17.**  
SAR raw data phase comparison of the algorithm proposed in Section 3.2 and the time domain algorithm.

the azimuth cut and **Figure 17(b)** is the range cut. It can be seen that the phase errors of the proposed algorithm and the time-domain algorithm are both minimal, proving the effectiveness of the proposed algorithm.

## 4. Conclusion

In this chapter, we present a fast echo simulation algorithm of airborne striped SAR with trajectory error in squint condition, the fast echo simulation algorithm of airborne stripmap SAR with antenna attitude jitter and trajectory error, and the fast echo simulation algorithm of airborne stripmap SAR with attitude jitter and trajectory error in squint condition. From the comparison between the proposed hybrid-domain echo algorithm and the time-domain algorithm, it can be seen that the phase error slice is within a reasonable range, but the hybrid algorithm runs faster than the time-domain simulation by using FT, which is conducive to the simulation of large scenes.

## Acknowledgements

The author would like to thank Professor Kunshan Chen for his support in reviewing. This work is supported by Innovation Funds of China Aerospace Science and Technology (No. Y-Y-Y-FZLDTX-20).

## Author details

Yuhua Guo<sup>1,2\*</sup>, Shichao Jin<sup>1,2</sup> and Yuhong Guo<sup>3</sup>


1 State Key Laboratory of Space-Ground Integrated Information Technology, Beijing, China

2 Beijing Institute of Satellite Information Engineering, Beijing, China

3 Department of Mathematics, Taiyuan Normal University, Jinzhong, China

\*Address all correspondence to: yuhuaguo321@163.com

## IntechOpen

© 2021 The Author(s). Licensee IntechOpen. This chapter is distributed under the terms of the Creative Commons Attribution License (<http://creativecommons.org/licenses/by/3.0>), which permits unrestricted use, distribution, and reproduction in any medium, provided the original work is properly cited. 

## References

- [1] Fornaro G. Trajectory deviations in airborne SAR: Analysis and compensation. *IEEE Transactions on Aerospace and Electronic Systems*. 1999; **35**:997-1009. DOI: 10.1109/7.784069.
- [2] Mori A, De Vita F. A time-domain raw signal simulator for interferometric SAR. *IEEE Transactions on Geoscience and Remote Sensing*. 2004; **42**: 1811-1817, DOI:10.1109/TGRS.2004.832242.
- [3] Dogan O, Kartal M. Time domain SAR raw data simulation of distributed targets. 2010:1-11. DOI: 10.1155/2010/784815.
- [4] Zhang F, Hu C, Li W, Hu W, Li HC. Accelerating time-domain SAR raw data simulation for large areas using multi-GPUs. *IEEE Journal of selected topics in applied earth observations and remote sensing*. 2014; **7**:3956-3965. DOI: 10.1109/JSTARS.2014.2330333.
- [5] Franceschetti G, Schirizzi G. a SAR processor based on two dimensional FFT code. *IEEE Transactions on Aerospace and Electronic Systems*. 1990; **26**:356-365. DOI: 10.1109/7.53462.
- [6] Franceschetti G, Miliaccio M, Riccio D, Schirizzi GSARAS. A SAR raw signal simulator. *IEEE Transactions on Geoscience and Remote Sensing*. 1992; **30**:110-123. DOI: 10.1109/36.124221.
- [7] Khwaja AS, Ferro-Famil L, Pottier E. Efficient stripmap SAR raw data generation taking into account sensor trajectory deviations. *IEEE Transactions on Geoscience and Remote Sensing Letters*. 2011; **8**:794-798. DOI: 10.1109/LGRS.2011.2111411
- [8] Franceschetti G, Iodice A, Perna S, Riccio D. SAR sensor trajectory deviations: Fourier domain formulation and extended scene simulation of raw data. *IEEE Transactions on Geoscience and Remote Sensing*. 2006; **9**:2323-2334. DOI: 10.1109/TGRS.2006.873206.
- [9] Franceschetti G, Iodice A, Perna S, Riccio D. Efficient simulation of airborne SAR raw data of extended scenes. *IEEE Transactions on Geoscience and Remote Sensing*. 2006; **10**:2851-2860. DOI: 10.1109/TGRS.2006.875786.
- [10] Diao GJ, Xu XJ. Fast algorithm for SAR raw data simulation with large squint angles. *Journal of Electronics and Information Technology*. 2011; **33**: 684-689. DOI: 10.3724/SP.J.1146.2010.00498
- [11] Franceschetti G, Guida R, Iodice A, Riccio D, Ruello G. Efficient Simulation of hybrid stripmap/spotlight SAR raw signals from extended scenes. 2004; **42**: 2385-2396. DOI: 10.1109/TGRS.2004.834763
- [12] Xu W, Deng YK. Efficient Spaceborne TOPS mode SAR raw signal simulation of extended scenes. *Journal of Electronics and Information Technology*. 2012; **34**:187-193. DOI: 10.3724/SP.J.1146.2011.00216.
- [13] Boerner E, Balss U, Eineder M. Simulation of distributed spotlight raw data from X-SAR/STRM stripmap data. In: *International Geoscience and Remote Sensing Symposium*. 2004; **3**:1770-1773
- [14] Xu W, Huang PP, Deng YK. Efficient sliding spotlight SAR raw signal simulation of extended scenes. *EURASIP Journal of Advances in Signal Processing*. 2011; **52**:1-7. DOI: 10.1186/1687-6180-2011-52.
- [15] Cimmino S, Giorgio F, Iodice A, Riccio D, Ruello G. Efficient spot-light SAR raw signal simulation of extended scenes. *IEEE Transactions on Geoscience and Remote Sensing*. 2003; **41**:2329-2337. DOI: 10.1109/TGRS.2003.815239



- [16] Domenico D, Gerardo DM, Antonio I, Daniele R, Giuseppe R. Efficient simulation of extended-scene SAR raw signals with any acquisition mode. In: International Geoscience and Remote Sensing Symposium. 2018. pp. 6715-6718
- [17] Shahrezaei IH, Kazerooni M, Fallah M. a complex target terrain SAR raw data generation and evaluation based on inversed equalized hybrid-domain algorithm processing. *Waves in Random and Complex Media*. 2017;**27**: 47-66. DOI: 10.1080/17455030.2016.1198062.
- [18] Sofiani R, Heidar H, Kazerooni M. An efficient raw data simulation algorithm for large complex marine targets and extended sea clutter in spotlight SAR. 2018;1223-1230. DOI: 10.1002/mop.31143
- [19] Cimmino S, Franceschetti G, Iodice A, Riccio D, Ruello G. Efficient spotlight SAR raw signal simulation of extended scenes. *IEEE Transactions on Geoscience and Remote Sensing*. 2003; **41**:2329-2337. DOI: 10.1109/TGRS.2003.815239
- [20] Jia L, Jia X, Xu XJ, He YH. SAR raw data generation for complex airport scenes. *Journal of Radars*. 2014;**3**: 565-573. DOI: 10.3724/SP.J.1300.2014.14071
- [21] Vandewal M, Speck R, Suess H. Efficient SAR raw data generation including low squint angles and platform instabilities. *IEEE Transactions on Geoscience and Remote Sensing Letters*. 2008;**5**:26-30. DOI: 10.1109/LGRS.2007.907419.
- [22] Tang XQ, Xiang MS, Wei L. SAR raw signal simulation accounting for antenna attitude variations. In: The IEEE International Geoscience and Remote Sensing Symposium (IGARSS). IEEE. 2009. pp. 613-616
- [23] Dogan O, Kartal M. Efficient stripmap-mode SAR raw data simulation including platform angular deviations. *IEEE Transactions on Geoscience and Remote Sensing Letters*. 2011;**8**:784-788. DOI: 10.1109/LGRS.2011.2112633
- [24] Fornaro G, Sansosti E, Lanari R, Tesauro M. Role of processing geometry in SAR raw data processing. *IEEE Transactions on Aerospace and Electronic Systems*. 2002;**38**:441-454. DOI: 10.1109/TAES.2002.1008978
- [25] Guo YH, Yang XY, Zhou. F F. a new motion compensation method for squinted stripmap synthetic aperture radar. *Journal of Computational Information Systems*. 2013;**9**:3453-3460. DOI: 10.12733/jcis5836.